22 April 2026

Activation of Hydroxylated Organic Cathodes Enables High-Rate Sodium Batteries

Gan Chen[1,2], Dong-Min Kim[1,2], Po-Yu Kung[2,3], Wenqian Xu[2,4], Ying Chen[2,5], Zeqian Zhang[2,5,6], Zhaoyang Chen[2,7,8], Youngmin Ko[1], Michael Yang[9], Jiqqi Wang[2,4], Kamila M. Wiaderek[2,4], Yan Yao[2,7,8], Yiyang Li[2,3], Brett A. Helms[1,2,10]

1. Molecular Foundry, Lawrence Berkeley National Laboratory
2. Energy Storage Research Alliance, Argonne National Laboratory
3. Materials Science and Engineering, University of Michigan
4. Advanced Photon Source, Argonne National Laboratory
5. Physical and Computational Sciences Directorate, Pacific Northwest National Laboratory
6. Department of Chemistry, University of Washington
7. Department of Electrical and Computer Engineering, University of Houston
8. Texas Center for Superconductivity at the University of Houston (TcSUH), University of Houston
9. Department of Chemistry, California
10. Materials Sciences Division, Lawrence Berkeley National Laboratory

Abstract

Organic cathodes are poised to lower transition metal burdens for producing sodium-ion and sodium metal batteries, yet most struggle to achieve premium performance due to low ionic and electronic conductivity. Maintaining a high concentration of mobile sodium ions in redox-active solids for fast ion transport at all states of charge remains a challenge, as does ensuring a high spin density to facilitate long-range electron transport. Here, we show that sodiation of hydroxylated organic cathode materials reconfigures molecular packing to simultaneously enhance electron and ion transport, yielding new phases whose electronic conductivity (10–3 S cm–1) surpass their progenitors by five orders of magnitude while also shortening the characteristic diffusion time for Na+ ions by 50%. Although sodiation can be performed ex situ, we find it more effective to carry it out in situ during formation, where progressive activation of redox sites coincides with a dramatic improvement in rate capability, enabling cells with specific capacity of 290 mAh g–1 at a discharge current density of 1500 mA g–1 and a remarkably low fade rate of only 0.021% per cycle over 1380 cycles. Sodiation emerges as a promising strategy to activate cathode material architectures toward high-power TWh-scalable energy storage systems.

Activation of Hydroxylated Organic Cathodes Enables High-Rate Sodium Batteries

Gan Chen,[1,2,†] *Dong-Min Kim,*[1,2,†] *Po-Yu Kung,* [2,3] *Wenqian Xu,* [2,4] *Ying Chen,* [2,5] *Zeqian Zhang,* [2,5,6] *Zhaoyang Chen,* [2,7,8] *Youngmin Ko*[1,‡], *Michael Yang,*[9] *Jiqqi Wang,* [2,4] *Kamila M. Wiaderek,* [2,4] *Yan Yao,* [2,7,8] *Yiyang Li,* [2,3] *Brett A. Helms*[1,2,10]*

[1]The Molecular Foundry, Lawrence Berkeley National Laboratory, Berkeley, California, 94720, United States

[2]Energy Storage Research Alliance, Argonne National Laboratory, 9700 South Cass Avenue, Lemont, IL 60439, USA

[3]Materials Science and Engineering, University of Michigan, Ann Arbor, Michigan 48109, United States

[4]X-ray Science Division, Advanced Photon Source, Argonne National Laboratory, Lemont, IL 60439, USA

[5]Physical and Computational Sciences Directorate, Pacific Northwest National Laboratory, Richland, Washington, 99352, U.S.A

[6]Department of Chemistry, University of Washington, Seattle, Washington, 98195, U.S.A

[7]Department of Electrical and Computer Engineering, University of Houston, Houston, Texas, 77204, U.S.A

[8]Texas Center for Superconductivity at the University of Houston (TcSUH), University of Houston, Houston, Texas, 77204, U.S.A

[9]Department of Chemistry, University of California, Berkeley, California, 94720, USA

[10]Materials Sciences Division, Lawrence Berkeley National Laboratory, Berkeley, California, 94720, United States

†Equally contributed to this work

‡Present address: Department of Chemistry, Sungkyunkwan University, Suwon, 16419, Republic of Korea

*Corresponding author (B. A. Helms): bahelms@lbl.gov

Abstract

Organic cathodes are poised to lower transition metal burdens for producing sodium-ion and sodium metal batteries, yet most struggle to achieve premium performance due to low ionic and electronic conductivity. Maintaining a high concentration of mobile sodium ions in redox-active solids for fast ion transport at all states of charge remains a challenge, as does ensuring a high spin density to facilitate long-range electron transport. Here, we show that sodiation of hydroxylated organic cathode materials reconfigures molecular packing to simultaneously enhance electron and ion transport, yielding new phases whose electronic conductivity (10^{-3} S cm^{-1}) surpass their progenitors by five orders of magnitude while also shortening the characteristic diffusion time for Na^+ ions by 50%. Although sodiation can be performed *ex situ*, we find it more effective to carry it out *in situ* during formation, where progressive activation of redox sites coincides with a dramatic improvement in rate capability, enabling cells with specific capacity of 290 mAh g^{-1} at a discharge current density of 1500 mA g^{-1} and a remarkably low fade rate of only 0.021% per cycle over 1380 cycles. Sodiation emerges as a promising strategy to activate cathode material architectures toward high-power TWh-scalable energy storage systems.

Introduction

Sodium batteries are promising candidates for TWh-scale energy storage owing to the natural abundance and low cost of sodium resources.[1-5] Deploying organic cathode materials[6-18] in these systems could further mitigate supply-chain risks, provided that molecular engineering is leveraged to access high capacities at high rates for emerging use cases, such as data centers.[19-21] However, many organic materials and electrodes comprising them suffer from poor electronic conductivity and sluggish ionic diffusivity, which contribute to slow redox kinetics, excessive cell polarization, and incomplete active material utilization that together constrain both capacity and rate capability.[22-24] Articulating a convergent design strategy that simultaneously improves electronic and ionic transport in organic cathodes remains top priority.[25]

Here, we advance 2,3-diamino-6,7,8,9-tetrahydroxyphenazine-1,4-dione (DTD) as a high-capacity organic cathode in sodium metal batteries (**Figure 1**), showcasing how its sodiation (Na-DTD) enhances both electronic conductivity and ionic diffusivity in composite electrodes, resulting in markedly improved redox kinetics and active material utilization over a well-recognized state-of-the-art organic cathode, *bis*-tetraaminobenzoquinone (TAQ). We tie the five-orders-of-magnitude increase in electronic conductivity (10^{-3} S cm^{-1}) and 50% shorter sodium-ion diffusion times within cathode particles to changes in solid-state molecular packing upon sodiation. Notably sodiation of hydroxylated organic cathode DTD proceeds spontaneously during electrochemical cycling, resulting in 60% increase in specific capacity over 60 cycles at a current density of ~100 mA g^{-1}. Moreover, once DTD has been activated *in-situ*, the rate capability of the cell supersedes those of both chemically sodiated Na-DTD and TAQ, such that a capacity of ~290 mAh g^{-1} is achievable at a discharge current density of 1500 mA g^{-1} with a remarkably low capacity fade rate of 0.021% per cycle across 1380 cycles in sodium metal cells. Through a combination of single-particle and full-cell electrochemical studies, we find that this superior rate

capability in electrochemically sodiated DTD over chemically sodiated Na-DTD is tied to differences in charge transfer resistance, suggesting that controlling the extent of sodiation during formation and activation may play a larger role than expected in the emergent behaviors.

Activation of hydroxylated organic cathodes via *in-situ* irreversible sodiation thus emerges as a compelling forward-looking design principle for simultaneously enhancing ionic and electronic transport, enabling long-lasting high-rate electrochemical energy storage systems with low critical minerals burdens. Rather than treating electronic conductivity and ionic diffusivity as competing parameters, sodiation reconfigures molecular packing and redox-active site connectivity to promote coupled Na^+ mobility and electronic spin delocalization, mitigating polarization and improving utilization under high-rate cycling. Our demonstration that this is possible with columnar-stacked DTD crystals suggests that layered cathode architectures may not be as critical as once held.[6,26,27] Our perspective reframes sodiation not simply as a passive consequence of cycling hydroxylated organic cathode materials,[7,28,29] but as a tunable materials parameter, where controlling the extent, spatial distribution, and chemical potential of Na^+ defines a new axis for tailoring materials properties. Furthermore, these gains must be realized in concert with amination strategies that stabilize organic radicals so that they maintain high spin density at all states of charge, which is essential for both short-range charge transfer at interfaces and long-range charge transport within composite cathodes. Together, controlled sodiation and targeted amination establish a cohesive framework for designing next-generation organic cathodes that achieve both fast redox kinetics and high capacity.

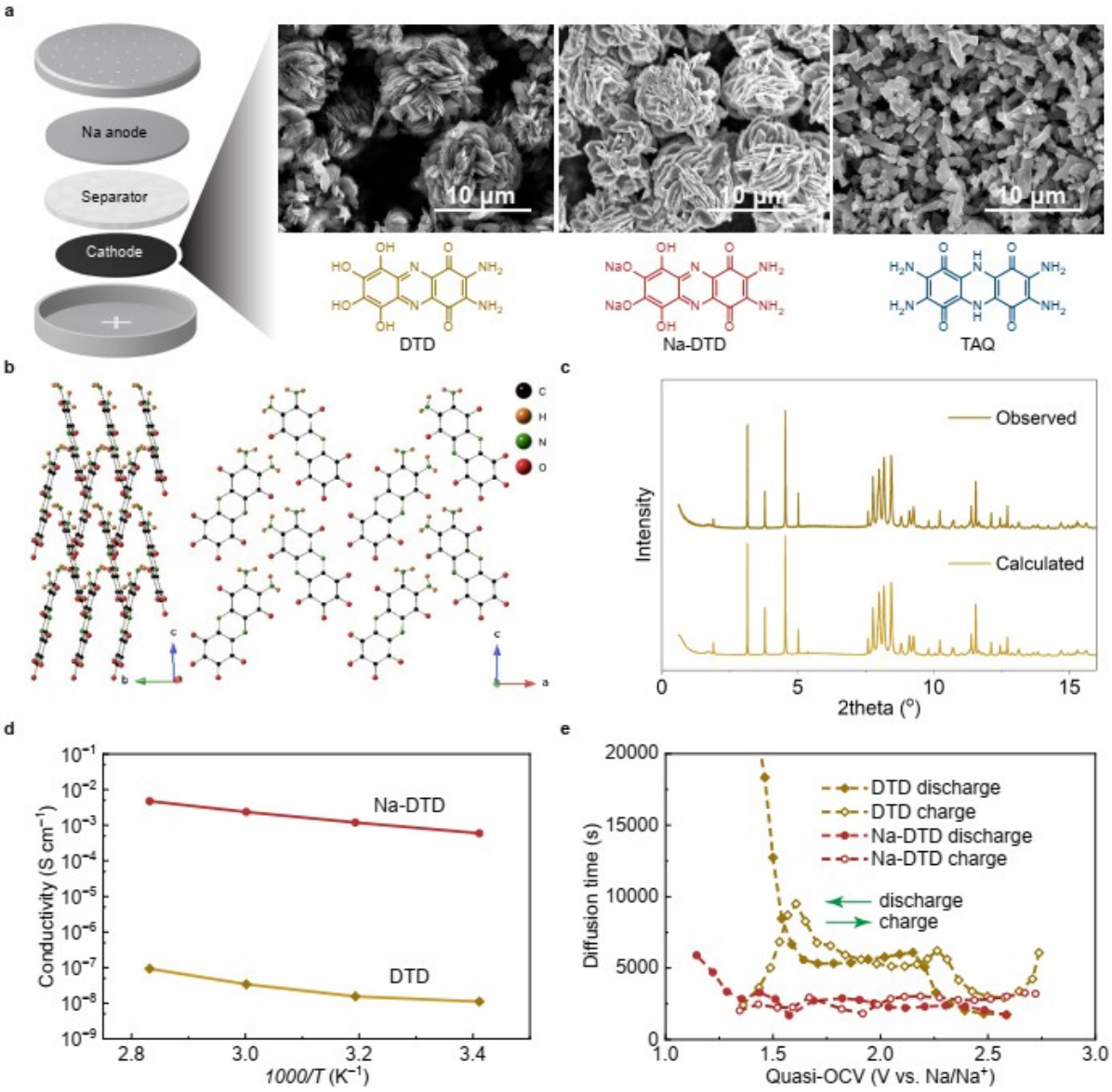

Figure 1. Sodiation of hydroxylated organic cathodes dramatically improves ion and electron transport. a, Schematic illustration of the sodium cell configuration incorporating the organic cathodes and SEM images & chemical structures of organic cathodes, DTD, Na-DTD and TAQ. **b**, Crystal structures of DTD and Na-DTD. **c**, Synchrotron PXRD refinement for DTD, X-ray wavelength is 0.46878 Å. **d**, Electronic conductivity for DTD and Na-DTD, measured with pelletized powders under 50 MPa. **e**, Na^+ diffusion time for DTD and Na-DTD, measured by GITT in coin cells.

Hydroxylated organic cathode design and chemical sodiation

It has been established that amination of organic cathodes opens the door to higher rates of electron transfer across interfaces and long-range electronic charge transport due to the apparent stabilization of organic radicaloid species across swings in state-of-charge, as typified by start-of-the-art TAQ-based active materials.[6,26,30-32] Yet, the concentration of sodium ions within TAQ is vanishingly small as the active materials are charged, which could compromise ionic diffusivity and redox kinetics.[8,29,33-36] We hypothesized that desymmetrization of organic active materials to feature a combination of oxidizable amines and ionizable hydroxyls could open the door to maintaining a concomitantly high concentration of spin and sodium ions in organic cathode materials, provided the functionality introduced did not result in cathode dissolution into the electrolyte after chemical or electrochemical salification. For example, if salification of hydroxyl functionality were irreversible and resulted in controlled placement of structural sodium ions in the solids, then the approach could provide for a general strategy to reduce active material dissolution and mitigate amorphization during repeated Na^+ insertion/extraction—all while maintaining fast ion and electron transport in cathode composites at all states of charge.

With this in mind, we designed and synthesized a tetrahydroxylated organic cathode—2,3-diamino-6,7,8,9-tetrahydroxyphenazine-1,4-dione (DTD)—in high yield (~80%) through a condensation reaction involving tetrahydroxy-1,4-quinone (THQ) and tetraamino-*para*-benzoquinone (TABQ). We confirmed the chemical structure of DTD by high resolution electrospray ionization mass spectrometry (**Supplementary Figure 1**), elemental analysis, and solid-state nuclear magnetic resonance (ssNMR). To enable the latter, we synthesized ^{15}N-labeled DTD and observed resonances from the central and amine nitrogen atoms with a 1:1 molar ratio in the ^{15}N direct-polarization NMR spectrum. In contrast, only the amine nitrogen signal was detected in the ^{1}H-^{15}N cross-polarization (CP) spectrum, signifying that the condensation product contains a pyrazine ring (**Supplementary Figures 2–3**). Because pyrazine ring formation requires tautomerization during condensation, it follows that the quinone originating from THQ

would rearomatize to a tetrahydroxyphenazine-1,4-done. We acquired the ^{13}C NMR spectrum for DTD (**Supplementary Figure 4**), which confirmed a diminished C=O peak by comparison to what has been reported TAQ.[26]

We then synthesized the chemically sodiated Na-DTD by treating DTD with excess 2.0 M NaOH methanol solution under ambient conditions. During the process, DTD remained a solid. Combining elemental analysis and inductively coupled plasma–optical emission spectroscopy (ICP-OES), we determined the sodium content to be 2.5~2.8 sodium per DTD molecule across different batches. As was the case with DTD, the ^{1}H-^{15}N CP NMR of ^{15}N-enriched Na-DTD showed no evidence of ^{1}H–^{15}N coupling at the central nitrogen, indicating that the pyrazine ring remained intact (**Supplementary Figure 2b**). Na-DTD did not exhibit observable ^{13}C signals, likely due to enhanced paramagnetic broadening combined with the intrinsically low sensitivity of natural-abundance ^{13}C NMR (**Supplementary Figure 4a**).

We found by scanning electron microscopy (SEM) and powder X-ray diffraction (PXRD) that DTD and Na-DTD were highly crystalline microflower solids **(Figure 1a–c**). The microflower assemblies were largely uniform in size and composed of interwoven nanosheets, providing large surface area and facilitating electrolyte accessibility. Single-crystal structures of DTD were solved through Rietveld refinement of high-quality synchrotron PXRD data (**Figure 1c**, **Supplementary Figure 5,** and **Supplementary Table 1**). Strong π–π interactions between DTD molecules give rise to their stacked packing into columns. The columnar slipped-stack offers rich opportunities for π–π orbital overlap, creating pathways for electrons to move through the crystal in the out-of-plane direction. The asymmetry in the molecular structure of DTD contributes to head-to-tail arrangements of DTD molecules and slipped stacking in the crystal, which favors the formation of more intermolecular hydrogen bonds. Na-DTD

displays a closely related topology, evidenced by similar diffraction patterns (**Supplementary Figure 6**), likely with Na^+ insertion accommodated through local coordination adjustments, rather than full lattice reconstruction. Such structural stability underscores the molecular design principle of integrating abundant intermolecular hydrogen bonding within redox-active motifs that tolerate ion insertion without collapse or tendency toward dissolution when in contact with liquid electrolyte.

Building on the structural motifs described above, we next examined how molecular packing governs coupled electronic and ionic transport in these materials, given that these properties are tightly correlated in organic crystals. In DTD the π–π stacking distance is 3.29 Å, while it is 3.18 Å for Na-DTD. This subtle change, however, dramatically impacts the out-of-plane electron transport pathway and the through-the-layer ion diffusion pathways. Na-DTD delivered a room-temperature electronic conductivity of ~10^{-3} mS s^{-1}, which represents a five-order-magnitude improvement in electronic conductivity compared to DTD across the measured temperature range. Such an improvement can be explained by the tighter π–π stacking[37,38] and much higher radical concentration in Na-DTD. We found that the radical concentration for DTD is 1.2%, while that for Na-DTD was 4.5% (**Supplementary Figure 7**). To understand how chemical sodiation influenced ion transport, we used a Galvanostatic Intermittent Titration Technique (GITT) to assess Na^+ diffusion times (**Supplementary Methods**) in organic cathodes at different states of charge while they were cycled in a coin cell using 1 M $NaPF_6$ 1,2-dimethoxyethane (DME, G1)/1-methoxy-2-(2-methoxyethoxy)ethane (DEGDME, G2) (1:1 *v*:*v*) as the liquid electrolyte. In most of the operating voltage window, the ion diffusion time for the chemically sodiated Na-DTD displayed a 50% decrease compared to the pristine DTD (**Figure 1e**). Na-DTD also showed relatively consistent ion-diffusion times across different states-of-charge, which is often beneficial for managing overpotentials during galvanostatic cycling. The fact that ion diffusion kinetics improved with a smaller π–π stacking distance might suggest a different ion diffusion mechanism from that of layered organic cathodes like TAQ.[6,26] The introduced structural sodium ions might serve as “bridge” between the stacked

column of DTD and enable ion migration pathways along the column edges, which reduces transport anisotropy and enabling more efficient coupling between ionic and electronic conduction. In short, introducing Na^+ in DTD enhances spin density, electronic delocalization between molecules in the packed solid, and flattens the energy landscapes for ion diffusion such that diffusion times are shorter and relatively constant at all states of charge. Together, these results suggest that Na-DTD should offer superior performance in sodium metal batteries where they are featured as organic cathode active materials.

Improved rate capability and cathode utilization upon *in-situ* activation

To establish how these structural and transport characteristics translate into electrochemical performance, we next evaluated the redox behavior and cycling characteristics of the active materials. We first investigated the redox behavior of the different active materials, followed by galvanostatic cycling and rate capability assessment for DTD, Na-DTD, and TAQ using coin cells comprised of organic cathode, GF/D glass fiber separator, Na metal and 1.0 M $NaPF_6$ in G1/G2(1:1 *v*:*v*) electrolyte (**Figure 2**). We examined active material redox behavior with cyclic voltammetry (CV) (**Supplementary Figure 8**). The voltammogram for DTD exhibited two peaks in current near 2.30 V and 1.45 V during discharge, which was followed by peaks in current at 2.20 V and 1.60 V during charge. On the other hand, Na-DTD exhibited more complex behavior, with peaks near 2.50 V, 1.95 V, 1.45 V, 1.20 V evidenced during discharge and peaks near 2.50 V, 2.30 V, 1.70 V, 1.45 V evidenced during charge. The complexity in redox behavior for Na-DTD was reminiscent of that for TAQ (discharge: 2.30 V, 2.18 V, 1.62V, 1.42 V, 1.32 V and charge: 2.73 V, 2.51 V, 2.34 V, 1.72 V, 1.60 V). This stark contrast in redox behavior suggests fundamental differences in solid-state electrochemical transformation among the cathode materials. Specifically, complex multi-step redox of Na-DTD indicates diverse local electrostatic environments within the lattice, which leads to multiple stable intermediate phases. This structural adaptability directly supports the underlying molecular design hypothesis. Furthermore, gradual structural reorganization is

expected to mitigate volumetric strain during redox, which would lead to enhanced stability over cycles.

We next compared galvanostatic cycling of DTD, Na-DTD, and TAQ at a discharge current density of 105 mA g^{-1} and a charge current density of 35 mA g^{-1} over 1.0–2.8 V (vs. Na/Na^+) (**Figure 2a–c**). We observed stable cycling for DTD, Na-DTD, and TAQ over 600, 1200, and 300 cycles, respectively, with maximum capacities of ~291, 235, and 288 mAh g^{-1}. These values correspond to active material utilizations of 83% for DTD, 79% for Na-DTD, and 82% for TAQ, relative to their theoretical capacities. Most notably, we found that DTD underwent a activation process *in situ*, during which the accessed capacity increased over ~60 cycles before stabilizing. In the first cycle, we measured a discharge capacity of 238 mAh g^{-1} for DTD but only 175 mAh g^{-1} upon charge, indicating that ~29% of Na^+ remained irreversibly inserted. We observed that this initial irreversibility coincides with a clear evolution in the voltage profile, which stabilizes in subsequent cycles and yields highly reversible charge–discharge behavior. We further analyzed these changes using *dQ*/*dV* profiles (**Supplementary Figure 9a**). In the first cycle, we identified discharge peaks near 2.30 V and 1.50 V; by the third cycle, the 2.30 V peak diminishes. As cycling proceeds from the 3^{rd} to the 100^{th} cycle, we observed peak shifts to 2.02 V and 1.35 V, along with a pronounced increase in the intensity of the 1.35 V feature. These results indicate that the irreversible capacity originates from redox processes near 2.30 V, while enhanced cathode utilization arises from redox activity near ~1.30–1.35 V. Importantly, we find that the evolved voltage profiles and *dQ*/*dV* features of activated DTD closely resemble those of Na-DTD (**Figure 2b, Supplementary Figure 9b**), demonstrating that DTD converges toward Na-DTD-like redox behavior during *in-situ* activation.

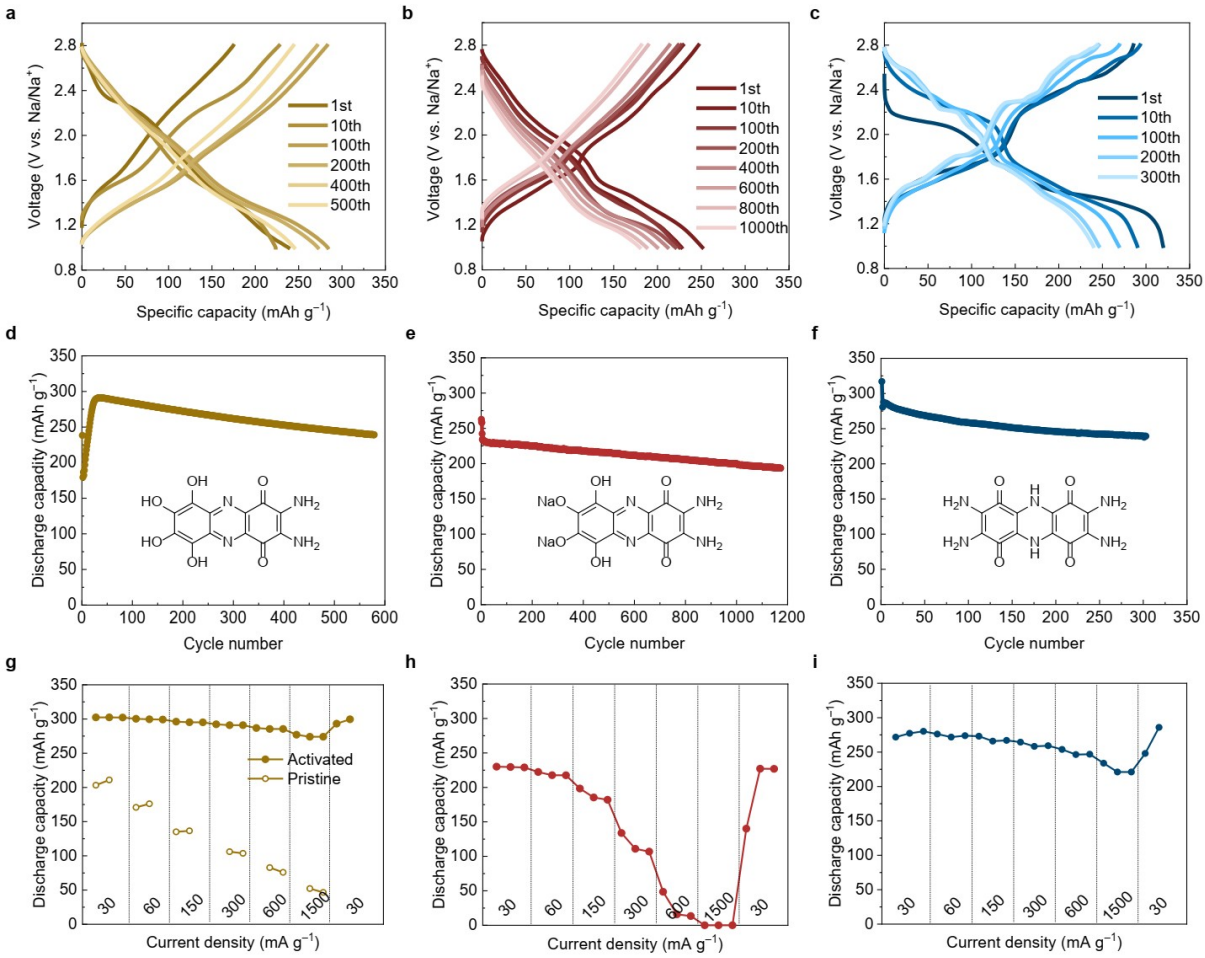

Figure 2. Hydroxylated organic cathodes undergo *in-situ* activation, improving active material utilization and rate capability. a–c, Voltage profiles, **d–f**, cycling performance at 35 mA g^{-1} charge and 105 mA g^{-1} discharge, **g–i**, rate capability with different current density of 30, 60, 150, 300, 600, and 1500 mA g^{-1}. (**a,d,g**) corresponds to DTD (yellow); (**b,e,h**) corresponds to Na-DTD (red); and (**c,f,i**) corresponds to TAQ (blue). Rate capability of pristine DTD was collected respectively after 1 formation cycle at each current density to minimize the influence of *in-situ* activation to the capacity delivered.

We next examined how *in-situ* activation of DTD influences cell performance by evaluating rate capability **(Figure 2g)**. We measured rate performance both before activation and after 60 activation cycles, using a baseline current density of 150 mA g^{-1}. Because DTD undergoes in-situ activation, we

assessed its pre-activation rate capability after a single formation cycle at 30 mA g^{-1}, followed by testing across increasing current densities. We found that *in-situ* activation of DTD dramatically enhances rate capability in Na metal cells: it delivers 275 mAh g^{-1} at a current density of 1500 mA g^{-1}. This capability not only surpasses that of pristine DTD, but also exceeds that of Na-DTD and TAQ, which deliver ~0.02 mAh g^{-1} and 221 mAh g^{-1}, respectively, at the same current density (**Figure 2h,i**). The poor performance of chemically sodiated Na-DTD was quite unexpected, given its higher electronic and ionic transport rates (**Figure 1d,e**). This divergence prompts fundamental questions regarding the structural origins of *in-situ* activation, the specific kinetic processes it modulates, and why activated DTD outperforms Na-DTD despite their similar apparent redox signatures.

In-situ activation of DTD via electrochemical sodiation

To answer these questions, we investigated the physical origins of *in-situ* DTD activation. We assessed emergent structural transformations via *ex-situ* XRD. The data were acquired after both discharge and charge in cycles 1 and 61 (**Figure 3a,b**). Diffraction peaks for DTD ranging between 10–16° shifted to lower angles immediately after the 1st discharge and are strikingly similar to chemically sodiated Na-DTD. These shifts were irreversible. Concurrently, new peaks emerged near 28°, which were also present in the diffraction pattern for chemically sodiated Na-DTD. These data lend further support to our claim that *in-situ* activation of DTD is tied to its progressive irreversible sodiation, which is apparent immediately after the first cycle. We further confirmed this by measuring the change in sodium content in the cathode composite by ICP-OES after 60 cycles (**Supplementary Figure 10**): the sodium content in DTD cathode increased from 1.8% to 18.8%, while that for Na-DTD showed only a slight increase from 16.1% to 17.6%. Likewise notable was the intensity and shifts of the diffraction peak near 28°, which is tied to π–π stacking. Not only did it become prominent with activation, it exhibited reversible shifts during charge and discharge. Thus, redox reactions contributing to DTD activation are affecting π–π stacking arrangements with increasing prevalence, but are ultimately reversible. In sharp contrast, the

same π–π stacking peak near 28° for chemically sodiated Na-DTD was relatively unaffected by state of charge. The discrepancy here between *in-situ* activated DTD and chemically sodiated Na-DTD in cells suggests that improvements in rate capability are linked to the energetics and reversibility of structural transformations involving π–π stacking arrangements. These transformations are likely tied to the redox peak near 1.30 V, which is markedly higher for *in-situ* activated DTD than for chemically sodiated Na-DTD (**Supplementary Figure 9a,b**). These findings highlight that electrochemical activation enables access to a dynamically evolving structural state that is not attainable through chemical sodiation.

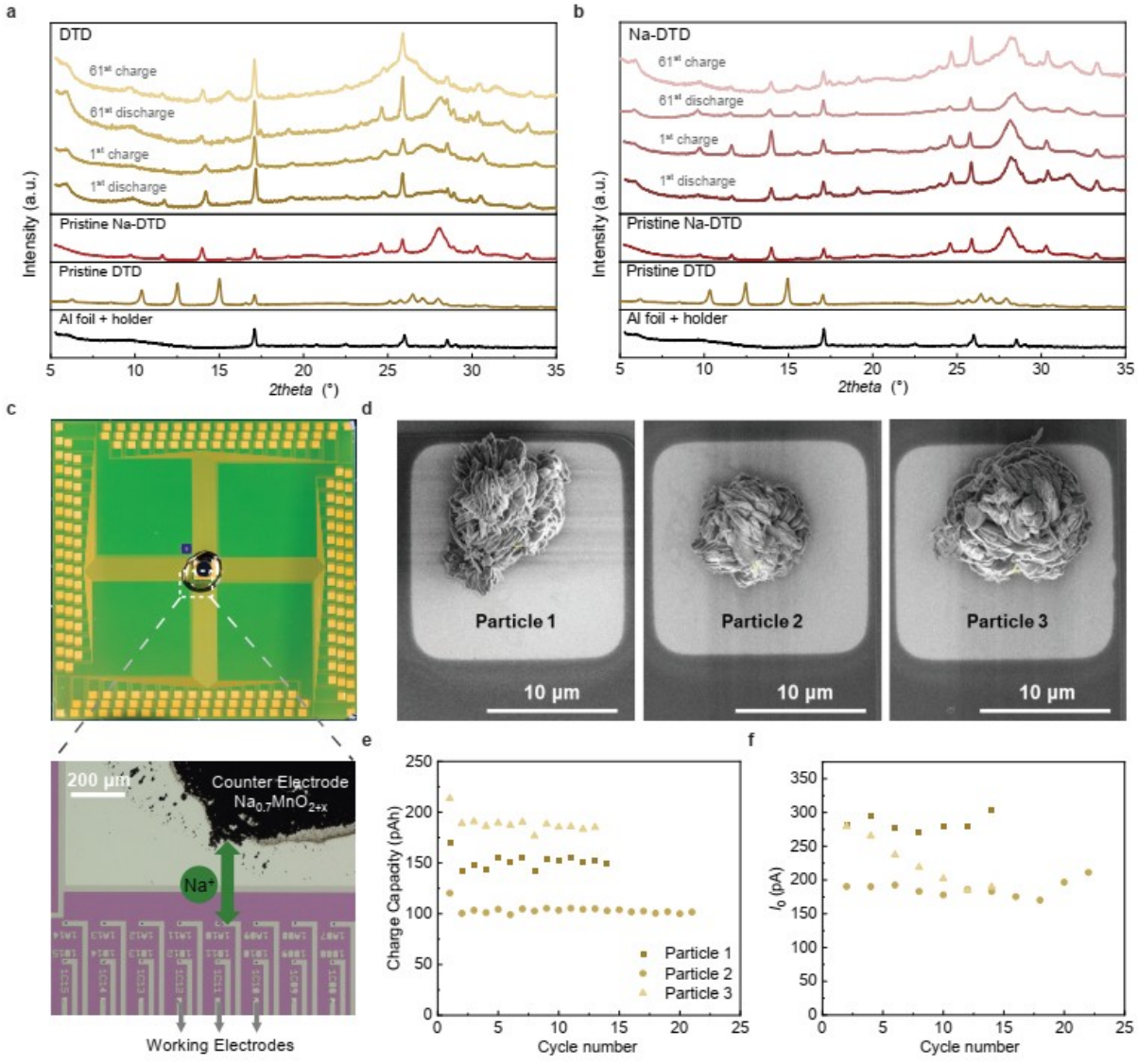

Figure 3. ***In-situ*** **activation of hydroxylated organic cathodes is tied to irreversible electrochemical**

sodiation. a, *ex-situ* XRD for DTD. **b**, *ex-situ* XRD for Na-DTD. **c**, Optical image of the microelectrode array. **d**, SEM images of Particle 1–3 on the working electrodes. **e–f**, Charge capacity (**e**), and exchange current (**f**) of the particles at C/10 in 1 M $NaClO_4$ in propylene carbonate.

To further isolate the change in Na^+ diffusion kinetics during DTD activation, we performed single-particle electrochemical measurements using a custom microelectrode array (**Figure 3c**), based on prior designs for inorganic cathode materials for Li-ion batteries.[39-41] Unlike the composite electrode architecture, the single-particle setup places the DTD particles directly on an Au current collector, substantially shortening the electronic transport pathway. Consequently, this approach enables the direct characterization of properties at the individual particle level, avoiding the ensemble-averaged response in conventional porous electrode measurements. The microelectrode array was designed with the 3 mm counter electrode positioned at the center and about sixty 15-μm Au working microelectrodes around it (**Supplementary Methods**). Each electrode was independently connected to peripheral contact pads at the chip margins, while the liquid electrolyte is confined to the center of the chip (**Figure 3c**). For this study, individual ~10-μm DTD particles were positioned onto 15-μm Au microelectrodes using a micromanipulator and fixed by e-beam Pt deposition. A $Na_{0.7}MnO_{2+x}$ (3.1 V vs Na/Na^+, **Supplementary Figure 11**) composite electrode served as both counter and reference electrode; and 1.0 M $NaClO_4$ in propylene carbonate was dispensed to encapsulate both the working and counter electrodes.

Single-particle electrochemical cycling (cycling profiles shown in **Supplementary Figures 12–14**) was conducted on three DTD particles at a rate of C/10 (**Figure 3d–f**). Potentiostatic Intermittent Titration Technique (PITT) was implemented during the discharge of every even-numbered cycle (**Supplementary Figures 15–17**) to determine the exchange current and characteristic diffusion time at 2.3 V vs. Na/Na^+. Notably, the exchange current (**Figure 3f**) remained essentially constant throughout the measurement,

whereas the diffusion time (**Supplementary Figure 18**) and Biot number (**Supplementary Figure 19**) showed slight decreases, indicating marginal improvements in ion transport. The average diffusion time (from 3 particles) dropped from ~32.3 min to ~26.2 min. while the average Biot number decreased from 32.6 to 25.9 during 14 cycles. These results indicate that ionic diffusion kinetics only improve slightly and the rate capability enhancement observed in composite electrodes cannot be purely driven by improvements in ion transport.

Our results also show that the charge capacity (for odd-numbered cycles) at the single-particle level did not increase with cycling (**Figure 3e**), a distinct departure from behavior observed in composite electrodes **(Figure 2a,d)**. We attributed this to the differences in cathode architecture. In our ~23-μm-thick composite cathodes, DTD particles are stacked above each other; while the carbon matrix improves the electrodes' electronic conductivity, its network is incomplete[42,43], forcing electrons to travel between the DTD particles. Increasing the electronic conductivity would substantially improve the rate capability. In contrast, our single-particle setup utilizes localized contact with an Au substrate via Pt deposition, necessitating an electron transport length of no more than 10 micron. As a result, an increase in the particle's electronic conductivity has a negligible impact on our single-particle measurement. This fundamental difference explains why the capacity and rate capability increases in composite electrodes are absent at the single-particle level, and supports electronic conductivity increasing upon *in-situ* activation as the origin of the improved electrochemical performance.

In-situ activation lowers energy barriers to charge transfer

To further investigate Na^+ ion diffusion and impedance in composite electrode, we assessed how Na^+ diffusion time and cell impedance differed before and after the activation cycles for DTD and Na-DTD using GITT (**Figure 4a**) and electrochemical impedance spectroscopy (EIS, **Figure 4b,c**). After 60 cycles

of activation, the Na^+ diffusion time of DTD in a composite electrode decreased and then stabilized throughout the voltage range, by comparison to that observed in the 1st cycle. Thus, activation allows Na^+ diffusion at faster steady rates at all states-of-charge. Moreover, the average diffusion time (across the whole voltage range) for *in-situ* activated DTD is 2233 ± 695 s, which is lower than that (2740 ± 781 s) of Na-DTD. In addition, the full cell impedance of DTD decreased after 60 cycles of activation compared to that after the 1st cycle, indicating a reduction in overall impedance of DTD full cell upon activation. In contrast, the impedance of Na-DTD increased dramatically after 60 cycles.

Motivated by these activation-induced changes in charge transfer resistance, we further compared high-rate cycling performance of cathode materials after 60 activation cycles (**Figure 4d–g**). Here, DTD delivered a capacity of ca. 290 mAh g^{-1} with remarkable stability over 1380 cycles at a discharge current density of 1500 mA g^{-1}. In contrast, Na-DTD delivered negligible capacity due to a high over-potential, while TAQ delivered a capacity of ~220 mAh g^{-1} for only up to 160 cycles under the same conditions. This demonstrates conclusively that *in-situ* activation of DTD is preferred, not only because of the improved rate capability, but also the cycling stability.

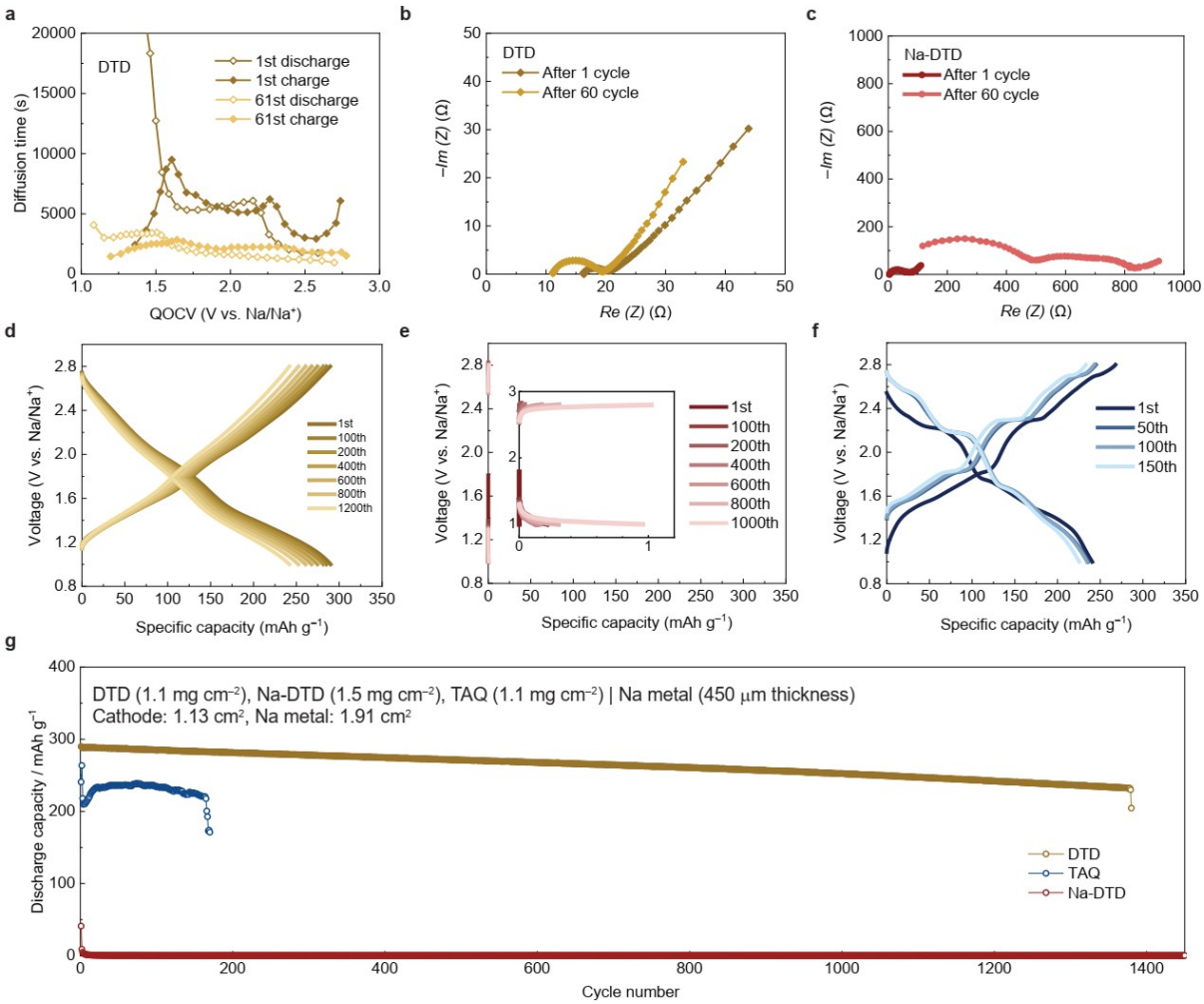

Figure 4. Sustaining lower charge transfer resistance helps hydroxylated organic cathodes maintain performance edge after *in-situ* sodiation. a, Characteristic diffusion time for DTD during 1st and 61st cycle. **b**,**c**, Cell impedance after 1 cycle and 60 cycles for DTD and Na-DTD. **d**–**g**, Voltage profiles (**d**–**f**) and cycling performance (**g**) of DTD, Na-DTD and TAQ with discharge current density of 1500 mA g^{-1}.

Taken together, these results establish that hydroxyl functionality, when introduced alongside amines in organic cathodes, can do more than simply enable sodiation—they can entirely reshape the coupled ion–electron transport landscape by modulating local coordination environments, stabilizing sodiated states, and facilitating percolating redox pathways. *In-situ* activation enabled by irreversible salification of

hydroxyl functionality during electrochemical cycling appears particularly advantageous, as it drives the system into a distinct thermodynamic and kinetic regime characterized by higher active material utilization and exceptional rate capability. This transformation over a progression of cycles gives rise to a dynamically reorganized structure—effectively a self-optimized Na-DTD phase—in which π–π stacking, redox energetics, and ion accessibility become more favorably aligned for rapid charge transfer. In doing so, DTD accesses behavior that exceeds that of state-of-the-art materials systems in sodium metal batteries.

Conclusion

Insights presented here point to a broader paradigm for organic cathodes in which molecular design enables not only improved performance, but also precise mechanistic and electrochemical control over coupled ion–electron transport phenomena and charge transfer across interfaces. By embedding structural ions and dynamic bonding motifs directly into redox-active supramolecular solids, one can enable adaptive transport networks that preserve redox accessibility and reversibility across a range of conditions. This paradigm invoking combinations of amine and hydroxy motifs on multi-electron redox-active organic molecules could become generalizable across Li-, Na-, and K-based cell chemistries and even extend to cathode design for solid-state batteries. Progress along these axes will necessarily require a deeper understanding of *in-situ* activation mechanisms and structurally explicit outcomes through a combination of theory, *in-situ,* and operando characterization[44,45] as new designs are proposed and validated toward long-life, high-power all-organic energy storage systems.

Acknowledgements

This work is funded by the Energy Storage Research Alliance "ESRA" (DE-AC02-06CH11357), an Energy Innovation Hub funded by the U.S. Department of Energy, Office of Science, Basic Energy Sciences. Work at the Molecular Foundry was supported by the Office of Science, Office of Basic Energy Sciences, of the U.S. Department of Energy under Contract No. DE-AC02-05CH11231, under proposal numbers MFP-10530 and MFP-10721. Part of this research was performed at 11-ID-B beamline on APS beam time award(s) (DOI: https://doi.org/10.46936/APS-191687/60015420) from the Advanced Photon Source, a U.S. Department of Energy (DOE) Office of Science user facility operated for the DOE Office of Science by Argonne National Laboratory under Contract No. DE-AC02-06CH11357. We thank Oliver Wright, Ambarneil Sasha, Mary C. Scott, and Peter Ercius for helpful discussions, identifying the *Pna2*$_1$ space group during crystal structure analysis.

Author contributions

G.C. and B.A.H. designed and B.A.H. directed the studies. G.C. carried out the material discovery and characterizations. D.K., Y.K., and M.Y. conducted electrochemical studies. P.K. and Y.L. carried out single particle measurements. W.X., J.W., and K.W. performed synchrotron XRD and crystal structure analyses. Z.Z and Y.C. performed EPR and solid-state NMR studies. Z.C. and Y.Y. measured cathode electronic conductivity. G.C., D.K., P.K., W.X., Y.C., Z.C., Y.L. and B.A.H. wrote first draft of the manuscript and all authors contributed to the final draft.

Competing interests

The authors declare the following competing interests: B.A.H., G.C., D.K., Y.Y., Z.C., W.X. and Y.C. are co-inventors on US provisional patent application 64/012,262 submitted by Lawrence Berkeley National Laboratory that covers DTD-based organic cathodes and their use in batteries. Y.Y. has a financial interest

in LiBeyond, LLC and Solid Design Instruments, LLC. The University of Houston reviewed and approved his relationship in compliance with its conflict-of-interest policy. B.A.H. has a financial interest in Cyklos Materials and Sepion Technologies.

Additional information

The data supporting the findings of this study are available within the paper and its Supplementary Information and Supplementary Data, and also from the authors upon reasonable request. Crystallographic data for DTD is available free of charge from the Cambridge Crystallographic Data Centre (www.ccdc.cam.ac.uk) under reference number 2547959. Source data are provided with this paper.

References

1 Hirsh, H. S. *et al.* Sodium-Ion Batteries Paving the Way for Grid Energy Storage. *Adv. Energy Mater.* **10**, 2001274, doi:https://doi.org/10.1002/aenm.202001274 (2020).

2 Sada, K., Darga, J. & Manthiram, A. Challenges and Prospects of Sodium-Ion and Potassium-Ion Batteries for Mass Production. *Adv. Energy Mater.* **13**, 2302321, doi:https://doi.org/10.1002/aenm.202302321 (2023).

3 Mariyappan, S., Desai, P., Morcrette, M. & Tarascon, J.-M. From lab to market with sustainable sodium-ion batteries. *Nat. Sustain.*, doi:10.1038/s41893-025-01701-x (2025).

4 Deysher, G. *et al.* Design principles for enabling an anode-free sodium all-solid-state battery. *Nat. Energy* **9**, 1161-1172, doi:10.1038/s41560-024-01569-9 (2024).

5 Zuo, W. *et al.* Layered Oxide Cathodes for Sodium-Ion Batteries: Storage Mechanism, Electrochemistry, and Techno-economics. *Acc. Chem. Res.* **56**, 284-296, doi:10.1021/acs.accounts.2c00690 (2023).

6 Chen, T. *et al.* High-Energy, High-Power Sodium-Ion Batteries from a Layered Organic Cathode. *J. Am. Chem. Soc.* **147**, 6181-6192, doi:10.1021/jacs.4c17713 (2025).

7 Zhang, C. *et al.* Plentiful abutting functional groups boosting sodium storage in a small molecule. *Energy Environ. Sci.* **17**, 6360-6367, doi:10.1039/D4EE02835J (2024).

8 Lee, M. *et al.* High-performance sodium–organic battery by realizing four-sodium storage in disodium rhodizonate. *Nat. Energy* **2**, 861-868, doi:10.1038/s41560-017-0014-y (2017).

9 Tang, M. *et al.* Tailoring π-Conjugated Systems: From π-π Stacking to High-Rate-Performance Organic Cathodes. *Chem* **4**, 2600-2614, doi:https://doi.org/10.1016/j.chempr.2018.08.014 (2018).

10 Shi, R. *et al.* Nitrogen-rich covalent organic frameworks with multiple carbonyls for high-performance sodium batteries. *Nat. Commun.* **11**, 178, doi:10.1038/s41467-019-13739-5 (2020).

11 Zeng, M. *et al.* A Crystalline Polymer Cathode for Sodium-Organic Batteries. *Angew. Chem. Int. Ed.* **64**, e202501134, doi:https://doi.org/10.1002/anie.202501134 (2025).

12 Kim, H. *et al.* High Energy Organic Cathode for Sodium Rechargeable Batteries. *Chem. Mater.* **27**, 7258-7264, doi:10.1021/acs.chemmater.5b02569 (2015).

13 Luo, W., Allen, M., Raju, V. & Ji, X. An Organic Pigment as a High-Performance Cathode for Sodium-Ion Batteries. *Adv. Energy Mater.* **4**, 1400554, doi:https://doi.org/10.1002/aenm.201400554 (2014).

14 Huang, J. *et al.* A Self-Healing Chemistry-Enabled Organic Cathode for Sustainable and Stable Sodium-Ion Batteries. *Small Struct.* **4**, 2300211, doi:https://doi.org/10.1002/sstr.202300211 (2023).

15 Kuan, H.-C. *et al.* A nitrogen- and carbonyl-rich conjugated small-molecule organic cathode for high-performance sodium-ion batteries. *J. Mater. Chem. A* **10**, 16249-16257, doi:10.1039/D2TA03953B (2022).

16 Yao, Y. *et al.* A Small-Molecule Organic Cathode with Extended Conjugation toward Enhancing Na+ Migration Kinetics for Advanced Sodium-Ion Batteries. *Small* **20**, 2401481, doi:https://doi.org/10.1002/smll.202401481 (2024).

17 Wang, S. *et al.* All Organic Sodium-Ion Batteries with Na4C8H2O6. *Angew. Chem. Int. Ed.* **53**, 5892-5896, doi:https://doi.org/10.1002/anie.201400032 (2014).

18 Fang, C. *et al.* A Metal–Organic Compound as Cathode Material with Superhigh Capacity Achieved by Reversible Cationic and Anionic Redox Chemistry for High-Energy Sodium-Ion Batteries. *Angew. Chem.* **129**, 6897-6901, doi:https://doi.org/10.1002/ange.201701213 (2017).

19 Kim, J. *et al.* Organic batteries for a greener rechargeable world. *Nat. Rev. Mater.* **8**, 54-70, doi:10.1038/s41578-022-00478-1 (2023).

20 Zhang, H. *et al.* Organic Cathode Materials for Sodium-Ion Batteries: From Fundamental Research to Potential Commercial Application. *Adv. Funct. Mater.* **32**, 2107718, doi:https://doi.org/10.1002/adfm.202107718 (2022).

21 Guo, Y., Ding, Z., Fang, Y. & Wu, D. in *2011 IEEE Global Telecommunications Conference - GLOBECOM 2011*. 1-5.

22 Qi, Y., Zhao, H., Chen, L. & Lei, Y. Solubility Challenges and Strategies for Organic Sodium-Ion Batteries: Status and Perspectives. *Small* **22**, 2412769, doi:https://doi.org/10.1002/smll.202412769 (2026).

23 Chen, Y., Fan, K., Gao, Y. & Wang, C. Challenges and Perspectives of Organic Multivalent Metal-Ion Batteries. *Adv. Mater.* **34**, 2200662, doi:https://doi.org/10.1002/adma.202200662 (2022).

24 Yu, Z., Wang, Y. & Luo, Z. Review on Redox-Active Organic Compounds for All-Organic Batteries. *Ind. Eng. Chem. Res.* **63**, 9619-9630, doi:10.1021/acs.iecr.4c00394 (2024).

25 Li, Z. *et al.* Practical lithium–organic batteries enabled by an n-type conducting polymer. *Nature* **651**, 100-106, doi:10.1038/s41586-026-10174-7 (2026).

26 Chen, T. *et al.* A Layered Organic Cathode for High-Energy, Fast-Charging, and Long-Lasting Li-Ion Batteries. *ACS Cent. Sci.* **10**, 569-578, doi:10.1021/acscentsci.3c01478 (2024).

27 Li, W. *et al.* Tuning electron delocalization of hydrogen-bonded organic framework cathode for high-performance zinc-organic batteries. *Nat. Commun.* **14**, 5235, doi:10.1038/s41467-023-40969-5 (2023).

28 Tuttle, M. R., Davis, S. T. & Zhang, S. Synergistic Effect of Hydrogen Bonding and π–π Stacking Enables Long Cycle Life in Organic Electrode Materials. *ACS Energy Lett.* **6**, 643-649, doi:10.1021/acsenergylett.0c02604 (2021).

29 Lee, J. & Park, M. J. Tattooing Dye as a Green Electrode Material for Lithium Batteries. *Adv. Energy Mater.* **7**, 1602279, doi:https://doi.org/10.1002/aenm.201602279 (2017).

30 Li, Z. *et al.* A Small Molecular Symmetric All-Organic Lithium-Ion Battery. *Angew. Chem. Int. Ed.* **61**, e202207221, doi:https://doi.org/10.1002/anie.202207221 (2022).

31 Chen, T. *et al.* High-rate, high-capacity electrochemical energy storage in hydrogen-bonded fused aromatics. *Joule* **7**, 986-1002, doi:https://doi.org/10.1016/j.joule.2023.03.011 (2023).

32 Tan, B., Chen, T., Wang, J. & Dincă, M. A metal-free cathode for high-performance potassium-ion batteries under ambient and sub-zero temperatures. *Watt* **1**, 5, doi:10.1007/s44503-026-00005-1 (2026).

33 Song, Z. *et al.* A quinone-based oligomeric lithium salt for superior Li–organic batteries. *Energy Environ. Sci.* **7**, 4077-4086, doi:10.1039/C4EE02575J (2014).

34 Zhang, Y. *et al.* Ionically conducting Li- and Na-phosphonates as organic electrode materials for rechargeable batteries. *Chem. Sci.* **16**, 1819-1825, doi:10.1039/D4SC07732F (2025).

35 Zhao, Q. *et al.* Oxocarbon Salts for Fast Rechargeable Batteries. *Angew. Chem. Int. Ed.* **55**, 12528-12532, doi:https://doi.org/10.1002/anie.201607194 (2016).

36 Wang, Y. *et al.* High-Performance Polymeric Lithium Salt Electrode Material from Phenol–

Formaldehyde Condensation. *ACS Appl. Mater. Interfaces* **13**, 37289-37298, doi:10.1021/acsami.1c11687 (2021).

37 Xie, L. S., Alexandrov, E. V., Skorupskii, G., Proserpio, D. M. & Dincă, M. Diverse π–π stacking motifs modulate electrical conductivity in tetrathiafulvalene-based metal–organic frameworks. *Chem. Sci.* **10**, 8558-8565, doi:10.1039/C9SC03348C (2019).

38 Dou, J.-H. *et al.* Atomically precise single-crystal structures of electrically conducting 2D metal–organic frameworks. *Nat. Mater.* **20**, 222-228, doi:10.1038/s41563-020-00847-7 (2021).

39 Min, J., Gubow, L. M., Hargrave, R. J., Siegel, J. B. & Li, Y. Direct measurements of size-independent lithium diffusion and reaction times in individual polycrystalline battery particles. *Energy Environ. Sci.* **16**, 3847-3859, doi:10.1039/D3EE00953J (2023).

40 Min, J., Suk, W., Wong, S. C. Y. & Li, Y. Single-Particle Electrochemical Cycling Single-Crystal and Polycrystalline NMC Particles. *Adv. Funct. Mater.* **34**, 2410241, doi:https://doi.org/10.1002/adfm.202410241 (2024).

41 Suk, W., Min, J., Liu, T. & Li, Y. Microelectrode Arrays for Electrochemical Cycling of Individual Battery Particles. *Chem. Mater.* **37**, 1788-1797, doi:10.1021/acs.chemmater.4c02736 (2025).

42 Zhu, C., Usiskin, R. E., Yu, Y. & Maier, J. The nanoscale circuitry of battery electrodes. *Science* **358**, eaao2808, doi:10.1126/science.aao2808 (2017).

43 Oh, Y. *et al.* Enhanced Electrical Connectivity in High Energy Density Single-Crystal NCA Electrodes via Polycrystalline Blending Design. *ACS Appl. Mater. Interfaces* **17**, 28094-28102, doi:10.1021/acsami.5c01515 (2025).

44 Peng, C. *et al.* Reversible multi-electron redox chemistry of π-conjugated N-containing heteroaromatic molecule-based organic cathodes. *Nat. Energy* **2**, 17074, doi:10.1038/nenergy.2017.74 (2017).

45 Vizintin, A. *et al.* Probing electrochemical reactions in organic cathode materials via in operando infrared spectroscopy. *Nat. Commun.* **9**, 661, doi:10.1038/s41467-018-03114-1 (2018).